

LOCAL SIMULATIONS OF THE MAGNETO-ROTATIONAL INSTABILITY IN CORE-COLLAPSE SUPERNOVAE

YOUHEI MASADA¹, TOMOYA TAKIWAKI², KEI KOTAKE^{2,3}, AND TAKAYOSHI SANO⁴

Accepted for publication in ApJ, Preprint typeset using L^AT_EXstyle

ABSTRACT

Bearing in mind the application to core-collapse supernovae, we study nonlinear properties of the magneto-rotational instability (MRI) by means of three-dimensional simulations in the framework of a local shearing box approximation. By changing systematically the shear rates that symbolize the degree of differential rotation in nascent proto-neutron stars (PNSs), we derive a scaling relation between the turbulent stress sustained by the MRI and the shear-vorticity ratio. Our parametric survey shows a power-law scaling between the turbulent stress ($\langle\langle w_{\text{tot}} \rangle\rangle$) and the shear-vorticity ratio (g_q) as $\langle\langle w_{\text{tot}} \rangle\rangle \propto g_q^\delta$ with its index $\delta \sim 0.5$. The MRI-amplified magnetic energy has a similar scaling relative to the turbulent stress, while the Maxwell stress has slightly smaller power-law index (~ 0.36). By modeling the effect of viscous heating rates due to the MRI turbulence, we show that the stronger magnetic fields or the larger shear rates initially imposed lead to the higher dissipation rates. For a rapidly rotating PNS with the spin period in milliseconds and with strong magnetic fields of 10^{15} G, the energy dissipation rate is estimated to exceed $10^{51} \text{ erg sec}^{-1}$. Our results suggest that the conventional magnetohydrodynamic (MHD) mechanism of core-collapse supernovae is likely to be affected by the MRI-driven turbulence, which we speculate, on one hand, could harm the MHD-driven explosions due to the dissipation of the shear rotational energy at the PNS surface, on the other hand the energy deposition there might be potentially favorable for the working of the neutrino-heating mechanism.

Subject headings: instabilities—rotation— supernova: magnetic fields — stars: proto-neutron stars

1. INTRODUCTION

Numerical simulations of magnetohydrodynamic (MHD) stellar explosions have started already in the early 1970's shortly after the discovery of pulsars (LeBlanc & Wilson 1970; Bisnovatyi-Kogan et al. 1976; Müller & Hillebrandt 1979; Symbalisty 1984). However, it is rather only recently that the MHD studies come back to the front-end topics in the supernova research followed by a number of extensive MHD simulations (e.g., Ardeljan et al. 2000; Yamada & Sawai 2004; Kotake et al. 2004a,b; Obergaulinger et al. 2006a,b; Burrows et al. 2007; Cerdá-Durán et al. 2007; Takiwaki et al. 2009; Scheidegger et al. 2010; Takiwaki & Kotake 2011; Obergaulinger & Janka 2011, and Kotake et al. (2006, 2012a,b) for recent reviews). Main reasons for this activity are observations indicating very asymmetric explosions (Wang et al. 2001, 2002), and the interpretation of magnetars (Duncan & Thompson 1992; Lattimer & Prakash 2007) and gamma-ray bursts (e.g., Woosley & Heger 2006; Yoon & Langer 2005) as a possible outcome of the magnetorotational core-collapse of massive stars.

The MHD mechanism of stellar explosions relies on the extraction of rotational free energy of collapsing progen-

itor core via magnetic fields. Hence a high angular momentum of the core is preconditioned for facilitating the mechanism (Meier et al. 1976). Given (a rapid) rotation of the pre-collapse core, there are at least two ways to amplify the initial magnetic fields to a dynamically important strength, namely by the field wrapping by means of differential rotation that naturally develops in the collapsing core, and by the so-called magneto-rotational instability (MRI, see Balbus & Hawley 1998).

Akiyama et al. (2003) were the first to point out that the interfaces surrounding the nascent protoneutron stars (PNSs) quite generally satisfy the instability criteria for the MRI. Therefore any seed magnetic fields can be amplified exponentially in the differentially rotating layers, much faster than the linear amplification due to the field wrapping. After the MRI enters to the saturated state, the field strength might reach $\sim 10^{15-16}$ G, which is high enough to affect the supernova dynamics. Not only to amplify the magnetic fields, the MRI plays a crucial role also in operating the MHD turbulence (see Hawley et al. 1995; Balbus & Hawley 1998; Masada et al. 2006). The turbulent viscosity sustained by the MRI can convert a fraction of the shear rotational energy to the thermal energy of the system. Thompson et al. (2005) suggested that the additional energy input by turbulent viscous heating can help the neutrino-driven supernova explosion. Followed by the exponential field amplification and the additional heating, a natural outcome of the magnetorotational core-collapse may be the formation of energetic bipolar explosions, which might be observed as the so-called hypernovae (see Tanaka et al. 2009 and references therein).

Here it is noted that bipolar explosions obtained in the previous MHD supernova simulations mentioned

¹ Department of Computational Science, Graduate School of System Informatics, Kobe University; Nada, Kobe 657-8501; E-mail: ymasada@harbor.kobe-u.ac.jp

² Center for Computational Astrophysics, National Astronomical Observatory of Japan, 2-21-1 Osawa, Mitaka, Tokyo, 181-8588, Japan

³ Division of Theoretical Astronomy, National Astronomical Observatory of Japan, 2-21-1, Osawa, Mitaka, Tokyo, 181-8588, Japan; E-mail: kkotake@th.nao.ac.jp

⁴ Institute of Laser Engineering, Osaka University, 1-1, Yamadaoka, Suita, Japan; E-mail: sano@ile.ac.jp

above are not driven by the MRI, but predominantly by the field wrapping, assuming very strong pre-collapse magnetic fields ($\gtrsim 10^{12}\text{G}$) in general. The growth rate of MRI-unstable modes depends on the product of the initial field strength and the wavenumber of the mode. In the case of the canonical initial fields ($\sim 10^9\text{G}$) as predicted by recent stellar evolution models (Heger et al. 2005), the fastest growing modes are estimated to be at most a few meters in the collapsing iron core (Obergaullinger et al. 2009). Unfortunately however, it is still computationally too expensive to resolve those scales in the global MHD simulations, typically more than two orders-of-magnitudes smaller than the typical finest grid size. To reveal the nature of the MRI, local simulations focusing on a small part of the MRI-unstable regions are expected to be quite useful as traditionally studied in the context of accretion disks (see Balbus & Hawley 1998).

Obergaullinger et al. (2009) were the first to report their numerical simulations to study the linear growth and nonlinear properties of the MRI in the supernova environment. To ease a drawback of the local shearing box simulation, they employed the shearing disk boundary conditions by which the global radial density in the vicinity of the equatorial region in the supernova core can be taken into account. By performing such a *semi-global* simulation systematically in two (2D) and three dimensions (3D), they derived scaling laws for the termination of the linear growth of the MRI. As estimated in Akiyama et al. (2003), the MRI was shown to amplify the seed fields exceeding 10^{15}G . These important findings may open several questions that motivate us to join in this effort, such as how the non-linear properties as well as the scaling laws could be changed by other parameters yet unexplored in the supernova context (that we are going to explain in the next paragraph), and whether the viscous heating maintained by the MRI turbulence could or could not affect the supernova mechanism.

A fundamental and long-lasting issue regarding the MRI itself is to understand the features of the MRI in the non-linear phase and to specify which physical quantities determine the saturation levels of the MRI. So far, extensive efforts have been paid to measure parameter dependence of the MRI-sustained turbulence by means of numerical simulations. It was reported that the amplitude of the turbulent stress maintained by the MRI depends on the net value of the initial magnetic field and the gas pressure of the system, that is

$$w_{\text{tot}} \propto B^\xi P^\zeta, \quad (1)$$

where ξ and ζ are the power law indices (see also Blackman et al. 2007 for the scaling relation between the turbulent stress and the plasma beta). Hawley et al. (1995) found that the saturation amplitude depends on the field strength when the system is penetrated initially by a uniform vertical field ($w_{\text{tot}} \propto B$), but is independent of the initial field strength if there is no net magnetic flux in the system (see also Sano et al. 2004). However, in the density stratified system, it is recently suggested that the turbulent stress increases almost linearly with magnetic energy of the net vertical field ($w_{\text{tot}} \propto B^2$; Suzuki et al. 2010; Okuzumi & Hirose 2011). A weak dependence of the gas pressure on the MRI turbulence was found by Sano et al. (2004): $\zeta \simeq 1/4$ for models with

initial net-zero magnetic flux and $\zeta \simeq 1/6$ in the system penetrated by uniform magnetic field. The physical mechanisms responsible for these parameterdependences remain an issue under considerable debate.

In the stellar interior condition, such as in the supernova core, it should be important to understand how the degree of differential rotation of the PNS could affect the nonlinear properties of the MRI. This is because the shear rate at the PNS surface ($q \equiv -d\ln\Omega/d\ln r$ with Ω and r representing the angular velocity and radius, respectively) is time- and location- dependent unlike accretion disks in which a force balance between the centrifugal force and gravity is generally maintained.

In this work, we study the MRI-driven turbulence and their nonlinear properties by performing three-dimensional simulations in the framework of a local shearing box approximation. By changing systematically the shear rates that symbolize the degree of differential rotation in nascent PNSs, we specifically study how the nonlinear properties of the MRI-driven turbulence respond to it. Based on our numerical results, we estimate the energy deposition rate due to the viscous heating driven by the MRI and discuss its potential impacts on the supernova mechanism.

This paper opens with descriptions of the numerical methods and the initial settings in § 2. The numerical results are presented in § 3. Based on the numerical results, we then move on to address possible impacts of the MRI on the supernova mechanism in § 4 followed by discussions in § 5. We summarize our new findings in § 6.

2. NUMERICAL METHODS AND INITIAL SETTINGS

To study nonlinear properties of MRI, MHD equations are solved with a MPI-parallelized finite-difference code that was originally developed by Sano et al. (1998). The hydrodynamic part is based on the second-order Godunov scheme (van Leer 1979), which consists of Lagrangian and remap steps. The exact Riemann solver is modified to account for the effect of tangential magnetic fields. The field evolution is calculated with Consistent MoC-CT method and thus can avoid the numerical explosive instability appeared in the strong shear layer when the MoC method is adopted (Clarke 1996). The energy equation is solved in the conservative form. The advantages of our scheme are its robustness for strong shocks and the satisfaction of the divergence-free constraint of magnetic fields (Evans & Hawley 1988; Stone & Norman 1992).

We perform a series of 3D compressible MHD simulation by adopting the local shearing box model described in detail by Hawley et al. (1995). In the shearing box model, MHD equations are written in a local Cartesian frame of reference (x, y, z) co-rotating with the local portion of the stellar interior rotating at the angular velocity Ω corresponding to a fiducial radius in the cylindrical coordinate R . Then the coordinates are presented as $x = r - R$, $y = R\phi - \Omega t$, and z . The fundamental equations are written in terms of these coordinates within a small region surrounding the fiducial radius, in $\Delta r \ll R$,

$$\frac{\partial \rho}{\partial t} + \nabla \cdot (\rho \mathbf{v}) = 0, \quad (2)$$

$$\frac{\partial \mathbf{v}}{\partial t} + \mathbf{v} \cdot \nabla \mathbf{v} = -\frac{1}{\rho} \nabla \left(P + \frac{|\mathbf{B}|^2}{8\pi} \right) + \frac{(\mathbf{B} \cdot \nabla) \mathbf{B}}{4\pi\rho} - 2\Omega \times \mathbf{v} - 2q\Omega^2 x \hat{x}, \quad (3)$$

$$\frac{\partial \epsilon}{\partial t} + (\mathbf{v} \cdot \nabla) \epsilon = -\frac{P}{\rho} \nabla \cdot \mathbf{v} + \Phi, \quad (4)$$

$$\frac{\partial \mathbf{B}}{\partial t} = \nabla \times (\mathbf{v} \times \mathbf{B}), \quad (5)$$

where ϵ is the specific internal energy, and the other parameters have their usual meanings. The term $-2q\Omega^2 x \hat{x}$ in the momentum equation is the tidal expansion of the effective potential with a shear rate $q \equiv -d \ln \Omega / d \ln r$. Assuming the ideal gas, the pressure is given by $P = (\gamma - 1)\rho\epsilon$. The constant ratio of specific heats γ is considered for simplicity. We choose adiabatic gas with $\gamma = 5/3$ in this paper.

Since we focus on the local properties of the instability, we employ, as is described schematically in Figure 1, numerical grid representing a small portion of the convectively stable upper PNS below the neutrinosphere where the strong shear is naturally developed when the core-collapse (Akiyama et al. 2003; Thompson et al. 2005). Adopting the differentially rotating matter as an unperturbed state, the azimuthal velocity is given by $v_y = q\Omega x$ in the frame co-rotating with the velocity $R\Omega$. The radial force balance at the initial state is thus achieved between the Coriolis force and the tidal force which is the residual of the gravitational force mainly balancing with the background pressure gradient force. We discuss an applicability of our numerical results to the high-temperature and highly stratified plasma realized in the supernova environment and the effects of neutrino viscosity in §5.

We choose normalization with $\rho_0 = 1$, $\Omega = 10^{-3}$, and the computational domain has a radial size $L_x = 4$, an azimuthal size $L_y = 4$, and a vertical size $L_z = 1$. All of the runs use a uniform grid of $256 \times 256 \times 64$ zones. The initial field geometry is a uniform vertical magnetic field $\mathbf{B} = B_0 \mathbf{e}_z$ (net non-zero flux). We assume, for all the models, that the initial gas pressure is $P_0 = 5 \times 10^{-7}$ and the initial ratio of the gas and magnetic pressures, that is the plasma beta is $\beta_0 = 3200$. The pressure scale height is then $H_p = 1$, and is the same as the vertical box size. With this normalization, the initial field strength is $B_0 = 6.26 \times 10^{-5}$, yielding $v_{A0} = 1.77 \times 10^{-5}$, where $v_{A0} = B_0 / (4\pi\rho_0)^{1/2}$ is the Alfvén speed. Note that these non-dimensional parameters can be translated to the dimensional form suitable for supernova environments as $\rho = 10^{12} \text{ g cm}^{-3}$, $L = 10^2 \text{ cm}$, $\Omega = 10^2 \text{ rad sec}^{-1}$, $P = 5 \times 10^{25} \text{ dyn cm}^{-2}$, and $B = 2.2 \times 10^{12} \text{ G}$, which are summarized in Figure 1.

The initial characteristic wavelength of the MRI is given by $\lambda_{\text{MRI}} = 4\pi\eta v_{A0}/\Omega$ for ideal MHD case (Balbus & Hawley 1998), where $\eta \equiv 1/\sqrt{4q - q^2}$. Its ratio to the vertical box size is thus varied as $\lambda_{\text{MRI}}/L_z = 0.22\eta$ in our models. It is empirically known that, to gain a saturation level correctly, the MRI wavelength must be resolved at the saturated state by at least six grid zones (see Sano et al. 2004). Here we choose the initial setting which satisfies this empirical rule for all the models.

3. NUMERICAL RESULTS

3.1. A Fiducial Run

As a fiducial run, we examine temporal evolutions of the MRI in a model with a shear rate $q = 0.5$. Initial perturbations are introduced by giving a random velocity perturbations which are taken to have a zero mean value with a maximum amplitude of $|\delta v|/\sqrt{\gamma P_0/\rho_0} = 5 \times 10^{-3}$.

To characterize the properties of the MRI-driven turbulence, we pay particular attention to the magnetic energy, the Maxwell and Reynolds stresses, and total turbulent stress defined respectively by,

$$E_{\text{mag}} \equiv |\mathbf{B}|^2/8\pi, \quad (6)$$

$$w_M \equiv -B_r B_\phi/4\pi, \quad (7)$$

$$w_R \equiv \rho v_r \delta v_\phi, \quad (8)$$

$$w_{\text{tot}} \equiv w_M + w_R, \quad (9)$$

where δv_ϕ is the perturbed azimuthal velocity. Note that a volume average of these quantities is represented by single brackets (like $\langle E_{\text{mag}} \rangle$) and a time- and volume-average is by double brackets (like $\langle \langle E_{\text{mag}} \rangle \rangle$).

The thick, dash-dotted and dashed curves in Figure 2 show the temporal evolution of volume-averaged magnetic energy, Maxwell and Reynolds stresses normalized by the initial gas pressure P_0 . Note that the horizontal axis is normalized by the rotation period $t_{\text{rot}} \equiv 2\pi/\Omega = 6.28 \times 10^3$ (62.8 [ms] in dimensional form). In order for the demonstration of the typical evolution of the MRI, four time snapshots of the 3D structure of the radial magnetic field are visualized by means of volume rendering method in Figure 3. The color bar indicates the amplitude of the radial magnetic field, yellow for the positive values, and blue for the negative value. Panels (a)–(d) correspond to the snapshots at the times $t = 6t_{\text{rot}}$, $8t_{\text{rot}}$, $9t_{\text{rot}}$, and $11t_{\text{rot}}$ respectively.

As was described in the previous MRI studies for accretion disks with Keplerian rotation of $q = 1.5$, there are three typical evolutionary stages observed in our fiducial run, those are (i) linear exponential growth stage, (ii) transition stage, and (iii) nonlinear turbulent stage (Hawley & Balbus 1992; Hawley et al. 1995). Each stage is denoted by white, dark gray and light gray shaded regions in Figure 2.

In the stage (i), the channel structure of the magnetic field exponentially evolves and inversely cascades to the larger spatial scale with small structures merging as the magnetic field is amplified. This is because the channel mode of the MRI is an exact solution even for the nonlinear MHD equation (Goodman & Xu 1994). The temporal evolution of channel structures for the radial magnetic field is shown in the panel (a) of Figure 3.

Then in the stage (ii), the channel structure of the magnetic field is disrupted via the parasitic instability and/or magnetic reconnection at the transition stage (Goodman & Xu 1994; Obergaulinger et al. 2009). The channel disruption induces a drastic phase-shift from the coherent structure to the turbulent tangled structure of the field as is illustrated by the panels (b) and (c) of Figure 3. The magnetic energy stored in the amplified magnetic field is then converted to the thermal energy of the system.

Finally in the stage (iii), the nonlinear turbulent state emerges after the channel disruption is maintained long enough by the MRI-driven turbulence as is demonstrated in the panel (d) of Figure 3. Figure 2 shows that, at this stage, the turbulent Maxwell stress dominates the

Reynolds stress. It then converts the free energy stored in the differential rotation into the thermal energy of the system. The time- and volume-averaged total turbulent stress is saturated, in the fiducial model, at the level

$$\langle\langle w_{\text{tot}} \rangle\rangle \simeq 0.03P_0, \quad (10)$$

where the time average is taken over the saturated state from $50t_{\text{rot}}$ to $150t_{\text{rot}}$. It can be stated that the variation of the shear rate does not change the nonlinear properties of the MRI qualitatively.

In the shearing box model adopted in our study, such free energy is continuously injected from the radial boundaries. This is the reason why the turbulent stage powered by the MRI is maintained in our simulation. We discuss in § 5 the applicability of our numerical model in comparison with the shearing disk model employed in Obergaulinger et al. (2009).

3.2. Shear Rate Dependence

In the stellar interior, such as supernova cores, the rotation profile should be time- and location-dependent unlike the typical accretion disk which maintains a quasi-Keplerian rotation with the shear rate $q \simeq 1.5$. This is because the force balance is mainly achieved between the gravity and the pressure gradient force in the stellar interior. It should be important to study how the nonlinear properties of the MRI would respond to the change of the shear rate for estimating its impact on the supernova dynamics. The shear rates used in our parametric survey are listed in Table 1 with a few diagnostic quantities, the time- and volume-averaged Maxwell stress, Reynolds stress, magnetic energy and the ratio of Maxwell and Reynolds stresses, calculated from the numerical data.

Figure 4 shows the temporal evolution of the turbulent stress for the models with different shear rates. The grey, red, blue, orange, green and purple curves indicate the models with $q = 0.2, 0.5, 0.8, 1.2, 1.5$ and 1.8 respectively. Note that the other physical parameters are the same as those used in the fiducial run. It is found that both the linear growth rate and saturation amplitude of the turbulent stress become larger for the model with the larger shear rate. This trend can be recognized as well from the spatial structures of magnetic fields in the saturated state.

The volume rendered vertical magnetic field is visualized for the models with (a) $q = 0.5$ and (b) $q = 1.5$ in Figure 5. The time snapshot at $t = 100t_{\text{rot}}$ is chosen for both models. The red color corresponds to the positive value of the vertical field component and the blue is its negative value. The larger structure of the magnetic field is found to be generated for the model with the larger shear rate. The other components of the magnetic field have similar nonlinear properties.

Figure 6(a) exhibits the time- and volume-averaged Maxwell stress $\langle\langle w_M \rangle\rangle$ (red circles), Reynolds stress $\langle\langle w_R \rangle\rangle$ (blue squares), total stress $\langle\langle w_{\text{tot}} \rangle\rangle$ (green diamonds), and magnetic energy $\langle\langle E_{\text{mag}} \rangle\rangle$ (yellow triangles) as a function of parameter g_q , where $g_q \equiv q/(2 - q)$ is the ratio of vorticity $(2 - q)\Omega$ to the shear $q\Omega$ (hereafter called “shear-vorticity ratio”, see Abramowicz et al. 1996). Note that we take, at the saturated state, the temporal average of volume-averaged stresses and magnetic energy from $50t_{\text{rot}}$ to $150t_{\text{rot}}$ for models 1,2,3, and

from $100t_{\text{rot}}$ to $150t_{\text{rot}}$ for models 4,5,6,7. The black line, which is proportional to $g_q^{1/2}$, is plotted as a reference.

The Maxwell stress dominates the Reynolds stress for all the models we surveyed although the fraction of the Reynolds stress in the total stress increases with the shear-vorticity ratio g_q . It should be noted that the pure hydrodynamic shear instability develops in the system with the stronger shear of $q \geq 2$ (the so-called Rayleigh criterion, e.g., Chandrasekhar 1960). According to Hawley et al. (1999), the hydrodynamic turbulence is shown to change the properties of MRI turbulence when the Rayleigh criterion is satisfied (see also Workman & Armitage 2008). The Reynolds stress then exceeds the Maxwell stress. However, since $q \lesssim 2$ is generally satisfied in the vicinity of the PNSs (e.g., Kotake et al. 2004a; Obergaulinger et al. 2006a, 2009), the Maxwell stress is expected to dominate over the Reynolds stress and plays a major role in the turbulent heating process there.

A power-law relation between the shear-vorticity ratio and turbulent stress appears in this figure. The power law index δ of a scaling relation defined by

$$\langle\langle w_{\text{tot}} \rangle\rangle \propto g_q^\delta, \quad (11)$$

is about $1/2$ and the best fit is $\delta = 0.44$ among all the models in Figure 6(a). It would be interesting that the magnetic energy has a similar scaling relation to the turbulent stress, that is roughly $\langle\langle E_{\text{mag}} \rangle\rangle \propto g_q^{1/2}$ (the best fit is $\delta = 0.46$) although the Maxwell stress has a power law index of 0.36 (the best fit value) which is a bit smaller than that for the total stress. As was well known that the maximum growth rate of the MRI is linearly proportional to the shear rate q (that is $\gamma_{\text{max}} = q\Omega/2$), the scaling law of the turbulent stress we found here should be explained through the nonlinear properties of the MRI-driven turbulence.

3.3. Our Work versus Previous Studies

Thus far, the dependence of the non-linear properties of the MRI on the shear rate has been investigated only in models whose net magnetic flux is set to zero (Brandenburg et al. 1996; Abramowicz et al. 1996; Hawley et al. 1999; Ziegler & Rüdiger 2001; Pessah & Chan 2008). These previous studies found the stronger dependence of the turbulent stress on the shear-vorticity ratio g_q (or rather shear rate q itself) which is in contrast to the weak dependence ($\delta = 1/2$ see equation (11)) obtained here in the case of the non-zero magnetic flux.

Abramowicz et al. (1996; hereafter ABL96) numerically evaluated the MRI-sustained turbulent stress for different values of the shear-vorticity ratio in the stratified system with net zero magnetic flux. They found that the turbulent stress is roughly represented by a linear dependence on the shear-vorticity ratio, that is $\delta = 1.0$ of equation (11). On the other hand, the numerical results obtained by Ziegler & Rüdiger (2001; hereafter ZR01) with a similar numerical setting as that adopted in ABL96 suggested that the existence of a relation $\langle\langle w_{\text{tot}} \rangle\rangle \propto q$ [i.e., $\propto 2g_q/(g_q + 1)$] in contrast to the finding of ABL96.

The dependence of the turbulent stress on the shear rate was studied comprehensively by Hawley et al. (1999;

hereafter HBW99) using unstratified shearing box model with net zero magnetic flux. They found that the vorticity $((2 - q)\Omega)$ limits hydrodynamic turbulence and strongly reduces the Reynolds stress at around $q = 0$. In contrast, the shear $(q\Omega)$ promotes turbulence, and thus the Maxwell and Reynolds stresses both are enhanced with increasing the shear rate. Since the q -dependence of the Reynolds stress is much stronger than that of the Maxwell stress, the stress ratio diminishes with increasing q . When extracting the data from Figure 10 of HBW99, the time- and volume-averaged turbulent stress seems to behave as $\langle\langle w_{\text{tot}} \rangle\rangle \propto g_q^{1/2}$ (the best fit is $\delta = 0.55$).

Liljeström et al. (2009; hereafter LKKBL09) studied, using local shearing box model with net zero magnetic flux, the nonlinear properties of MRI-driven turbulence with varying shear rate. By fitting numerical data listed in Table 1 of LKKBL09, the turbulent stress has strong q -dependence like as that of ABL96 and behaves approximately as $\langle\langle w_{\text{tot}} \rangle\rangle \propto g_q$ (the best fit is $\delta = 0.9$).

A theoretical model for the saturation of the Maxwell and Reynolds stresses in MRI turbulence was developed by Pessah et al. (2006; hereafter PCP06) in light of the similarities exhibited by the linear regime of the MRI and the turbulent state. On the basis of linear theory, they formulate a predictor function about the ratio of the Maxwell and Reynolds stresses at the saturated state, that is $\langle\langle w_M \rangle\rangle / \langle\langle w_R \rangle\rangle = (2 + g_q)/g_q$ [$= (4 - q)/q$ in the other form]. LKKBL09 found that the relation for the stress ratio derived by PCP06 predicts similar behavior, but provides a few times smaller ratio than that computed from their numerical results. The local closure model developed by Ogilvie (2003) rather could reproduce numerical results of LKKBL09 quite well.

For the comparison between our work and the previous studies, the ratio of the time- and volume-averaged Maxwell and Reynolds stresses is plotted as a function of the shear-vorticity ratio g_q in Figure 6(b). The blue squares correspond to our result, the green crosses show the numerical data of HBW99, the orange triangles are the result of LKKBL09, and the red circles present the result of ZR01. A power law relation of $\langle\langle w_M \rangle\rangle / \langle\langle w_R \rangle\rangle \propto g_q^{-3/4}$ is shown by the solid line for the reference. The theoretical model of the stress ratio developed by PCP06 is traced by the dashed line. Remember that the previous studies, as was summarized above, provided different g_q -dependences of the turbulent stress. The non-zero magnetic flux is imposed only in our work though the shearing box approximation is adopted in all the models. The stress ratio of HBW99 is calculated by extracting the data from Figure 10 of HBW99.

The stress ratio decreases with the increase of the shear-vorticity ratio g_q for all the models. This suggests that the Reynolds stress has generally a stronger g_q -dependence than that of the Maxwell stress. As LKKBL09 discussed, the model stress ratio of PCP06 predicts similar behavior, but gives a few times smaller value than that obtained by all the numerical models especially in the range $0.2 \lesssim g_q \lesssim 10$. It is a bit surprising that the stress ratio is similar among three works except HBW99 although they predict different power-law relations between the turbulent stress and the shear-

vorticity ratio. The stress ratio is roughly represented by a power-law relation $\langle\langle w_M \rangle\rangle / \langle\langle w_R \rangle\rangle \propto g_q^{-3/4}$ in the range of $0.5 \lesssim q \lesssim 1.8$. These similar nonlinear characteristics lied behind the MRI-driven turbulent flows suggest that the stress ratio might be one of key parameters for validating the nonlinear saturation mechanism of the MRI.

4. IMPACTS ON THE SUPERNOVA EXPLOSION

As taken in Thompson et al. (2005), the α -description (Shakura & Sunyaev 1973) conventionally used in the context of accretion disks is the simplest way to model the turbulent heating. However, it is quite uncertain whether the prescription is really applicable to the supernova problem. Based on our numerical results, we hope to reexamine whether the turbulent heating due to the MRI could have impacts on the explosion mechanism.

Combining our result with scaling relations of the turbulent stress described by equation (1), the heating rate maintained by the MRI turbulence can be expressed as,

$$\begin{aligned} \epsilon_{\text{MRI}} &= \langle\langle w_{\text{tot}} \rangle\rangle q \Omega \\ &= \epsilon_0 \left(\frac{B}{B_0} \right)^\xi \left(\frac{P}{P_0} \right)^\zeta \left(\frac{g_q}{g_{q0}} \right)^\delta \left(\frac{q}{q_0} \right) \left(\frac{\Omega}{\Omega_0} \right) \quad (12) \end{aligned}$$

where ϵ_0 represents the turbulent heating rate at the reference state with B_0 , P_0 , g_{q0} , q_0 , and Ω_0 . The power law indices are positive values depending on the presence of the stratification or net magnetic flux, and are expected to be $\xi = 1 \sim 2$ (Hawley et al. 1995; Sano et al. 2004; Suzuki et al. 2010; Okuzumi & Hirose 2011), $\zeta = 1/4 \sim 1/6$ (Sano et al. 2004), and $\delta = 1/2 \sim 1$ (see §3.3).

When choosing the physical parameters adopted in the fiducial model as the reference state, that is $B_0 = 2.2 \times 10^{12}$ G, $P_0 = 5 \times 10^{25}$ erg cm $^{-3}$, $\Omega_0 = 10^2$ rad s $^{-1}$, $g_{q0} = 0.33$ and $q = 0.5$, we can estimate, from equation (10), the reference heating rate as $\epsilon_0 = 0.03 P_0 q_0 \Omega \simeq 10^{26}$ erg cm $^{-3}$ sec $^{-1}$ (see §3.1 for the fiducial run).

We make a crude estimate of the volume in which the MRI-driven turbulence becomes active as $V_{\text{MRI}} = 4\pi R^2 h \simeq 10^{21}$ cm 3 $R_7^2 h_6$, where $R_7 = R/10^7$ cm is typical radius of the PNS normalized by 10^7 cm, and $h_6 = h/10^6$ cm is the typical radial thickness of the MRI-active layer normalized by 10^6 cm. Then the energy releasing rate $L_{\text{MRI}} \equiv \epsilon_{\text{MRI}} V_{\text{MRI}}$ becomes,

$$\begin{aligned} L_{\text{MRI}} &\simeq 10^{47} R_7^2 h_6 \text{ erg sec}^{-1} \times \\ &\left(\frac{B}{B_0} \right)^\xi \left(\frac{P}{P_0} \right)^\zeta \left(\frac{g_q}{g_{q0}} \right)^\delta \left(\frac{q}{q_0} \right) \left(\frac{\Omega}{\Omega_0} \right), \quad (13) \end{aligned}$$

Since we are interested in the MRI in the post-bounce stage of core-collapse supernovae, the gas pressure in the neutrino opaque upper PNSs is a known parameter and should be $P = 10^{31}$ erg cm $^{-3}$. When applying the typical gas pressure at the post-bounce phase to equation (13) with remaining the other parameters, the energy releasing rate is slightly enhanced and becomes $L_{\text{MRI}} \simeq 10^{48}$ erg sec $^{-1}$ almost independent of ζ . The magnetic field strength and the rotation profile are fully unknown parameters in the supernova environment. These thus determine whether the MRI-sustained turbulent heating can assist the supernova explosion or not.

The energy releasing rate due to the MRI-driven turbulence L_{MRI} is mapped in Figure 7 as functions of the

magnetic field strength B and the shear rate q . Panels (a) and (b) show the models with the weakest parameter dependence of $\xi = 1$ and $\delta = 1/2$, while panels (c) and (d) are for the models with the strongest parameter dependence of $\xi = 2$ and $\delta = 1$. The slow rotation of $\Omega = \Omega_0$ is assumed in left panels and the fast rotation of $\Omega = 10\Omega_0$ is in right panels. The green, blue and red dashed curves correspond to the energy releasing rates 10^{50} , 10^{51} , and 10^{52} erg sec $^{-1}$ respectively. The darker color gives the higher energy releasing rate. Note that the gas pressure is fixed to be 10^{31} erg cm $^{-3}$ and then the weak gas pressure dependence of the MRI-driven turbulence is neglected here for the simplicity.

The dark shaded parameter space provides the larger energy releasing rate than about 10^{51} erg sec $^{-1}$ which should assist the supernova explosion.⁵ The MRI-turbulent heating then have a minor effect on the supernova explosion in the unshaded parameter space which provides the luminosity $L_{\text{MRI}} \ll 10^{51}$ erg sec $^{-1}$.

It is fairly obvious that the stronger magnetic field or the larger shear rate yields the higher energy release due to the MRI, and thus makes a greater contribution on the supernova explosion. When considering the moderate shear of $q \simeq 1$ and angular velocity of $\Omega = \mathcal{O}(10^2)$ rad sec $^{-1}$ which are plausible for the supernova environment (Ott et al. 2006), a strong magnetic field of $B \gtrsim 10^{15}$ G is required for the MRI-assisted supernova explosion in the case with the weakest parameter dependence of $\xi = 1$ and $\delta = 1/2$ [Panels (a) and (b)]. The magnetic field weaker than 10^{13} G can drive the MRI-driven turbulence strong enough for assisting the explosion when the MRI turbulence depends strongly on the physical parameters B and q [see Panels (c) and (d)].

The nonlinear MRI studies employing shearing box model might suggest that non-canonical post-bounce states, such as having strong magnetic field and/or large spin rate, must be developed for prompting MRI-assisted supernova explosion. It may be tempting to implement those phenomenological heating rates as sub-grid model into the global MHD supernova simulations to see the outcomes. However, before that, it is more important to conduct a more extensive nonlinear study of the MRI over a wider parameter range and/or using more realistic numerical setting in order to precisely fix the scaling relations.

5. DISCUSSION

5.1. Effects of Neutrino Viscosity on MRI

In the neutrino opaque upper PNSs where we have a great interest on in this paper, the neutrino viscosity was shown to suppress the growth of the MRI when the viscous dissipation timescale of a typical MRI mode becomes shorter than the typical evolution time of the MRI (see Masada et al. 2007; Masada & Sano 2008). This is

⁵ The typical timescale of neutrino-driven explosions observed in the recent supernova simulations is $\gtrsim 300$ ms after bounce (e.g., Marek & Janka 2009; Suwa et al. 2010, 2012; Müller et al. 2012). So the energy deposition could be as high as 10^{50} erg when the MRI-driven turbulence maintains the heating of 10^{51} erg sec $^{-1}$. Since the explosion energy of core-collapse supernovae is estimated as 10^{51} erg, the turbulent heating due to the MRI is expected to play an important role in assisting explosion when $L_{\text{MRI}} \gtrsim 10^{51}$ erg sec $^{-1}$.

equivalent to a condition

$$R_{\text{MRI}} \equiv \frac{v_A^2}{\nu\Omega} \lesssim 1, \quad (14)$$

where R_{MRI} is the Reynolds number for the MRI, v_A is the Alfvén velocity, Ω is the angular velocity and ν is the neutrino viscosity. This can be translated to the condition for the magnetic field

$$B \lesssim B_{\text{crit}} \equiv (4\pi\nu\rho\Omega)^{1/2}, \\ = 3.5 \times 10^{12} \rho_{12}^{1/2} \nu_{10}^{1/2} \Omega_2^{1/2} \text{ [G]}, \quad (15)$$

where ρ_{12} is the density normalized by 10^{12} g cm $^{-3}$, T_{11} is the temperature normalized by 10^{11} K, Ω_2 is the angular velocity normalized by 10^2 rad sec $^{-1}$, and ν is the neutrino viscosity normalized by 10^{10} cm 2 sec $^{-1}$ (see Masada et al. 2007 for the magnitude of the neutrino viscosity). Such enormous neutrino viscosity is plausible in the region just below the neutrinosphere where the strong differential rotation is developed.

Equation (15) means that if the magnetic field is weaker than the critical value even locally, the neutrino viscosity suppress the linear growth of the MRI. Longaretti & Lesur (2010) found that, in the non-resistive limit (i.e., highly conducting MHD fluid), the saturation level of the MRI does not be affected by the viscosity at the nonlinear stage despite the change of the linear growth rate. Their results might suggest that the effects of neutrino viscosity on the MRI-driven turbulence are only secondary in the supernova problem.

On one hand, when the magnetic field is weaker than the critical value B_{crit} , the linear growth of the MRI is suppressed and then the growth time of the fastest growing mode of the MRI t_{MRI} becomes

$$t_{\text{MRI}} = \left[\frac{2(2-q)}{q^2} \right]^{1/4} R_{\text{MRI}}^{-1/2} \Omega^{-1}, \quad (16)$$

(Masada & Sano 2008) in contrast to that for the case with larger magnetic field than the critical value given by $t_{\text{MRI}} = 2/(q\Omega)$. Figure 8 depicts the growth time of the fastest growing mode of the MRI as a function of the shear rate for the cases with $B \geq B_{\text{crit}}$ (solid line), $B = 10^{-2}B_{\text{crit}}$ (dashed line) and $B = 10^{-4}B_{\text{crit}}$ (dash-dotted line). We adopt the spin rate of $\Omega = 100$ rad sec $^{-1}$ in this figure.

Considering the spin rate and shear rate plausible for the nascent PNSs [$\Omega \simeq \mathcal{O}(10^2)$ rad sec $^{-1}$ and $q \simeq 1.0$], the growth time of the MRI becomes longer than 100 [ms], which is only marginally comparable to the typical timescale of neutrino-driven explosions observed in some recent supernova simulations (e.g., Marek & Janka 2009; Suwa et al. 2010; Takiwaki et al. 2012) when the magnetic field is much weaker than the critical value (dashed and dash-dotted curves). This suggests that the weaker field can not fully activate the MRI-driven turbulence within the dynamical timescale for the supernova explosion. From the viewpoint of the growth rate of the MRI as well as the saturation amplitude, we would require the large magnetic field and/or short spin period for the MRI-assisted supernova explosion.

5.2. Validity of Shearing Box Model

As described in Obergaulinger et al. (2009), the shearing box model can not treat the angular momentum

transport adequately. In this respect, the shearing disk model is indeed superior to the shearing box model. However due to the lack of a simulation technique which can appropriately take into account the feed back from the global fluid motions, it may not be settled yet (possibly even by the semi-global simulations) whether or not the MRI will really smear out the differential rotation in the supernova core. It may be possible that the shear energy tapped in the differentially rotating layers can be supplied continuously by extracting the thermal or gravitational energies. This is considered to be the case in the solar interior.

It is well known from the helioseismic observation that there exists a radial differential rotation in the upper part of the convectively stable radiative core (the so-called tachocline), where is suitable for the field wrapping via Ω -effect and the growth of the MRI (see Parfrey & Menou 2007; Masada 2011). Although the field wrapping process and/or MRI might be operated in the tachocline region, the radial shear persists secularly there. The hydrodynamic angular momentum transport processes, such as the meridional circulation and the convective motion (e.g., Ruediger 1989), are considered to sustain the differential rotation even if the magnetic tension force acts to smear out the differential rotation. In the post-bounce supernova core, the convectively stable regions are formed between the nascent neutron star and the stalled bounce shock, in which the neutrino cooling dominates over the neutrino heating (Janka 2001). We speculate that the activity of the MRI might be maintained there in the presence of the secular differential rotation, which is close to the situation assumed in the shearing box simulation.

To draw a robust conclusion, one should naturally need to include the density stratification as well as the effects of neutrino heating/cooling which determines the convective stability. This study is only a prelude to improve our modeling according to the long to-do lists one by one from now on, to understand the role of MRI on the supernova mechanism.

5.3. Magnetic Field Structure during Saturation

All our numerical models yield a turbulent, highly-tangled, magnetic field structure as the final saturated state. The turbulent flow and magnetic field persist during the saturation, and coherent channel structures appear only transiently. On the contrary, in Obergaulinger et al. (2009), large-scale coherent fields with efficient angular momentum transport emerge after the turbulent state and are maintained for some models with a uniform initial magnetic field using simulation boxes of small radial and azimuthal aspect ratios L_x/L_z and L_y/L_z .

The magnetic field structure during saturation would be determined by whether flow-driven and current-driven parasitic instabilities, which are responsible for the destruction of channel solutions of the MRI, can grow or not. Goodman & Xu (1994) predicted analytically that these parasitic modes require radial and azimuthal wavelengths larger than the vertical wavelength of the channel solution for being unstable (see also Latter et al. 2009; Pessah & Goodman 2009). The coherent channel structure emerging from developed turbulence is thus expected to evolve into the large-scale without the destruc-

tion by the parasites in the small simulation box.

Obergaulinger et al. (2009) numerically confirmed that small radial and azimuthal aspect ratios are required to maintain the large-scale structure of coherent magnetic fields at the saturated state (see Figs 23 and 24 in their paper). A stationary turbulent state with tangled magnetic fields appears even in the shearing disk model when the simulation box is large enough. The same trend regarding the magnetic field structure during saturation has been reported also in the shearing box simulation by Bodo et al. (2008) (see also Lesaffre et al. 2009).

As presented in § 2, we chose the computational domain having large aspect ratios of $L_x/L_z = L_y/L_z = 4$ for all the models. The parasitic instabilities thus can evolve without being affected by the box geometry, and then destroy coherent channels, yielding the less violent turbulent state continuously during the saturation. It should be stressed that, as studied by Sano & Inutsuka (2001), the recurrent formation of large-scale coherent fields can be observed in the saturated stage of our shearing box model when we reduce the simulation domain to that with small aspect ratios.

When the magneto-rotational core-collapse, the MRI-active region should be confined in the upper PNS with small radial and latitudinal extents of $\mathcal{O}(10^5\text{--}10^6)$ cm (see § 4). The azimuthal thickness of the MRI-unstable region is expected to be significantly larger than the radial and latitudinal ones. This geometry would inhibit the development of the coherent structure of magnetic fields by prompting parasitic instabilities, and lead persistently to a less violent MRI-driven turbulent state (cf., Obergaulinger et al. 2009). The turbulent, highly tangled magnetic field structure would be suitable for describing the MRI-active layer in the supernova cores.

6. SUMMARY

We performed a series of 3D compressible MHD simulation by adopting the local shearing box model. By changing systematically the magnitudes of the shear rate, we specifically studied how the nonlinear properties of the MRI-driven turbulence are controlled by the shear in the system. With applying our numerical results to the supernova environment, we examined the impact of the MRI on the supernova explosion mechanism. Our main findings are summarized as follows.

1. We could observe, in our fiducial run with $q = 0.5$, three typical evolutionary stages [(i) linear exponential growth stage, (ii) transition stage, and (iii) nonlinear turbulent stage] which are analogous to those found in previous works modeling accretion disks. This validates that the variation of the shear rate does not change linear and nonlinear properties of the MRI qualitatively. The turbulent stress was saturated at the level $\langle\langle w_{\text{tot}} \rangle\rangle \simeq 0.03P_0$ in our fiducial model.

2. Our parameter survey results in the power-law relation between the shear-vorticity ratio and turbulent stress. The power law index δ of $\langle\langle w_{\text{tot}} \rangle\rangle \propto g_q^\delta$ is about 1/2. The MRI-amplified magnetic energy has a similar scaling relation to the turbulent stress although the Maxwell stress has a power law index of 0.36.

3. It was found that the stress ratio, defined by $\langle\langle w_M \rangle\rangle / \langle\langle w_R \rangle\rangle$, decreases with the increase of the shear-vorticity ratio. In addition, the stress ratio calculated from our numerical results has the similar magnitude and

g_q -dependence with those obtained by previous works (LKKBL09 and ZR01) despite the different computational settings. In the range $0.5 \lesssim q \lesssim 1.8$, the stress ratio is roughly fitted by a power law relation $\langle\langle w_M \rangle\rangle / \langle\langle w_R \rangle\rangle \propto g_q^{-3/4}$.

4. The stronger magnetic field or the larger shear rate provides the higher energy release due to the MRI-driven turbulence. For a rapidly rotating PNS with the spin period in milliseconds and with strong magnetic fields of 10^{15} G, the energy dissipation rate is estimated to exceed 10^{51} erg sec $^{-1}$. Our results suggest that the conventional MHD mechanisms of core-collapse supernovae are likely to be affected by the MRI-driven turbulence, which we speculate, on one hand, could harm the MHD-driven explosions due to the dissipation of the shear rotational energy at the PNS surface, on the other hand the energy

deposition there might be potentially favorable for the working of the neutrino-heating mechanism.

We thank the anonymous referee for constructive comments. Numerical computations were carried on SX8 of Institute of Laser Engineering, Osaka University, and partly on XT4 and general common use computer system at the center for Computational Astrophysics, CfCA, the National Astronomical Observatory of Japan. This study was supported in part by the Grants-in-Aid for the Scientific Research from the Ministry of Education, Science and Culture of Japan (Nos. 19104006, 19540309, 20740150, 23540323, and 24740125) and by HPCI Strategic Program of Japanese MEXT.

REFERENCES

- Abramowicz, M., Brandenburg, A., & Lasota, J. 1996, MNRAS, 281, L21+
- Akiyama, S., Wheeler, J. C., Meier, D. L., & Lichtenstadt, I. 2003, Astrophys. J., 584, 954
- Ardeljan, N. V., Bisnovatyi-Kogan, G. S., & Moiseenko, S. G. 2000, Astron. Astrophys., 355, 1181
- Balbus, S. A. & Hawley, J. F. 1998, Reviews of Modern Physics, 70, 1
- Mueller, B., Janka, H.-T., & Heger, A. 2012, arXiv:1205.7078
- Bisnovatyi-Kogan, G. S., Popov, I. P., & Samokhin, A. A. 1976, Ap&SS, 41, 287
- Bodo, G., Mignone, A., Cattaneo, F., Rossi, P., & Ferrari, A. 2008, A&A, 487, 1
- Brandenburg, A., Nordlund, A., Stein, R. F., & Torkelsson, U. 1996, ApJ, 458, L45+
- Burrows, A., Dessart, L., Livne, E., Ott, C. D., & Murphy, J. 2007, Astrophys. J., 664, 416
- Burrows, A. & Lattimer, J. M. 1988, Phys. Rep., 163, 51
- Cerdá-Durán, P., Font, J. A., & Dimmelmeier, H. 2007, ArXiv Astrophysics e-prints
- Chandrasekhar, S. 1960, Principles of stellar dynamics, ed. Chandrasekhar, S.
- Clarke, D. A. 1996, ApJ, 457, 291
- Duncan, R. C. & Thompson, C. 1992, Astrophys. J. Lett., 392, L9
- Evans, C. R. & Hawley, J. F. 1988, ApJ, 332, 659
- Goodman, J. & Xu, G. 1994, ApJ, 432, 213
- Guan, X. & Gammie, C. F. 2009, ApJ, 697, 1901
- Hawley, J. F. & Balbus, S. A. 1992, ApJ, 400, 595
- Hawley, J. F., Balbus, S. A., & Winters, W. F. 1999, ApJ, 518, 394
- Hawley, J. F., Gammie, C. F., & Balbus, S. A. 1995, ApJ, 440, 742
- Heger, A., Woosley, S. E., & Spruit, H. C. 2005, Astrophys. J., 626, 350
- Janka, H. 2001, A&A, 368, 527
- Kotake, K., Sawai, H., Yamada, S., & Sato, K. 2004a, Astrophys. J., 608, 391
- Kotake, K., Yamada, S., Sato, K., Sumiyoshi, K., Ono, H., & Suzuki, H. 2004b, Phys. Rev. D, 69, 124004
- Kotake, K., Sato, K., & Takahashi, K. 2006, Reports of Progress in Physics, 69, 971
- Kotake, K., Takiwaki, T., Suwa, Y., et al. 2012, arXiv:1204.2330, accepted by Advances in Astronomy
- Kotake, K., Sumiyoshi, K., Yamada, S., et al. 2012, arXiv:1205.6284, accepted by Progress in Theoretical and Experimental Physics
- Latter, H.-N., Lesaffre, P., & Balbus, S. A. 2009, MNRAS, 394, 715
- Lattimer, J. M. & Prakash, M. 2007, Phys. Rep., 442, 109
- LeBlanc, J. M. & Wilson, J. R. 1970, Astrophys. J., 161, 541
- Lesaffre, P., Balbus, S. A., & Latter, H. 2009, MNRAS, 396, 779
- Lesur, G. & Ogilvie, G. I. 2010, MNRAS, 404, L64
- Longaretti, P. & Lesur, G. 2010, A&A, 516, A51+
- Marek, A. & Janka, H.-T. 2009, Astrophys. J., 694, 664
- Masada, Y. 2011, MNRAS Letters, 471, 331
- Masada, Y. & Sano, T. 2008, ApJ, 689, 1234
- Masada, Y., Sano, T., & Shibata, K. 2007, ApJ, 655, 447
- Masada, Y., Sano, T., & Takabe, H. 2006, ApJ, 641, 447
- Meier, D. L., Epstein, R. I., Arnett, W. D., & Schramm, D. N. 1976, Astrophys. J., 204, 869
- Müller, E. & Hillebrandt, W. 1979, A&A, 80, 147
- Obergaulinger, M., Aloy, M. A., Dimmelmeier, H., & Müller, E. 2006a, Astron. Astrophys., 457, 209
- Obergaulinger, M., Aloy, M. A., & Müller, E. 2006b, Astron. Astrophys., 450, 1107
- Obergaulinger, M., Cerdá-Durán, P., Müller, E., & Aloy, M. A. 2009, A&A, 498, 241
- Obergaulinger, M. & Janka, H.-T. 2011, ArXiv e-prints
- Parfrey, K. P. & Menou, K. 2007, ApJ, 667, L207
- Pessah, M. E. & Chan, C. 2008, ApJ, 684, 498
- Pessah, M. E. & Goodman, J. 2009, ApJ, 698, L72
- Ruediger, G. 1989, Differential rotation and stellar convection. Sun and the solar stars, ed. Ruediger, G.
- Sano, T. & Inutsuka, S. 2001, ApJ, 561, L179
- Sano, T., Inutsuka, S., & Miyama, S. M. 1998, ApJ, 506, L57
- Sano, T., Inutsuka, S., Turner, N. J., & Stone, J. M. 2004, ApJ, 605, 321
- Scheidegger, S., Kaeppli, R., Whitehouse, S. C., Fischer, T., & Liebendoerfer, M. 2010, ArXiv e-prints
- Shakura, N. I. & Sunyaev, R. A. 1973, A&A, 24, 337
- Stone, J. M. & Norman, M. L. 1992, ApJS, 80, 791
- Suwa, Y., Kotake, K., Takiwaki, T., Whitehouse, S. C., Liebendörfer, M. & Sato, K., 2010, PASJ, 62, L49
- Suwa, Y., Takiwaki, T., Kotake, K., et al. 2012, arXiv:1206.6101
- Symbalisty, E. M. D. 1984, Astrophys. J., 285, 729
- Takiwaki, T., Kotake, K., & Sato, K. 2009, Astrophys. J., 691, 1360
- Takiwaki, T., & Kotake, K. 2011, ApJ, 743, 30
- Takiwaki, T., Kotake, K., & Suwa, Y. 2012, ApJ, 749, 98
- Tanaka, M., Kawabata, K. S., Maeda, K., Iye, M., Hattori, T., Pian, E., Nomoto, K., Mazzali, P. A., & Tominaga, N. 2009, Astrophys. J., 699, 1119
- Thompson, T. A., Quataert, E., & Burrows, A. 2005, ApJ, 620, 861
- van den Horn, L. J. & van Weert, C. G. 1984, A&A, 136, 74
- van Leer, B. 1979, Journal of Computational Physics, 32, 101
- Wang, L., Howell, D. A., Höflich, P., & Wheeler, J. C. 2001, Astrophys. J., 550, 1030
- Wang, L., Wheeler, J. C., Höflich, P., Khokhlov, A., Baade, D., Branch, D., Challis, P., Filippenko, A. V., Fransson, C., Garnavich, P., Kirshner, R. P., Lundqvist, P., McCray, R., Panagia, N., Pun, C. S. J., Phillips, M. M., Sonneborn, G., & Suntzeff, N. B. 2002, Astrophys. J., 579, 671
- Woosley, S. E. & Heger, A. 2006, Astrophys. J., 637, 914
- Workman, J. C. & Armitage, P. J. 2008, ApJ, 685, 406
- Yamada, S. & Sawai, H. 2004, Astrophys. J., 608, 907
- Yoon, S.-C. & Langer, N. 2005, Astron. Astrophys., 443, 643
- Ziegler, U. & Rüdiger, G. 2001, A&A, 378, 668

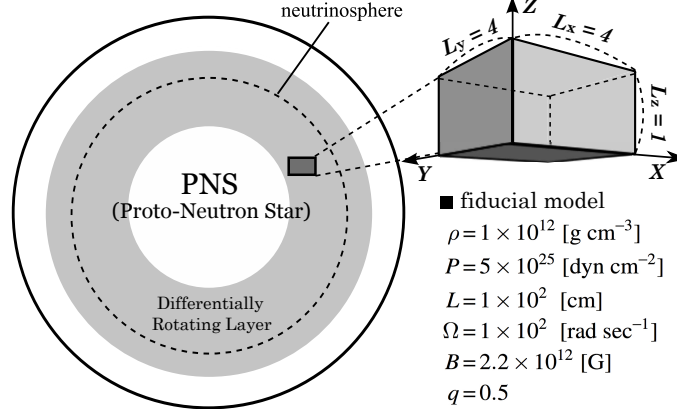


FIG. 1.— Schematic picture of the numerical setting in our calculations. The differentially rotating, neutrino-thick region below the neutrinosphere is focused (\simeq gray shaded region). The temporal evolution of the local portion of the upper proto-neutron stars is studied by the local shearing box model. The physical parameters adopted for our fiducial run are summarized in this figure.

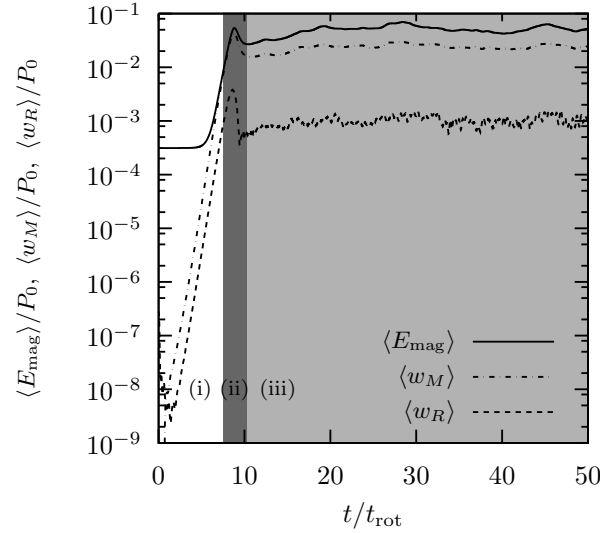


FIG. 2.— Temporal evolution of volume-averaged magnetic energy (solid), Maxwell stress (dash-dotted), and Reynolds stress (dashed) for the fiducial model with $q = 0.5$. The vertical and horizontal axes are normalized by initial gas pressure P_0 and rotation period t_{rot} respectively. Three typical evolutionary stages, that is (i) linear exponential growth stage, (ii) transition stage, and (iii) nonlinear turbulent stage are filled by white, dark gray and light gray shaded colors.

	shear rate q	$\langle \langle w_M \rangle \rangle / P_0$	$\langle \langle w_R \rangle \rangle / P_0$	$\langle \langle E_{\text{mag}} \rangle \rangle / P_0$	$\langle \langle w_M \rangle \rangle / \langle \langle w_R \rangle \rangle$
Model1	0.2	2.06×10^{-2}	1.96×10^{-4}	4.11×10^{-2}	1.05×10^2
Model2	0.5	2.86×10^{-2}	1.28×10^{-3}	6.57×10^{-2}	2.23×10^1
Model3	0.8	3.63×10^{-2}	3.09×10^{-3}	9.41×10^{-2}	1.18×10^1
Model4	1.0	3.99×10^{-2}	5.15×10^{-3}	1.09×10^{-1}	7.78×10^0
Model5	1.2	5.38×10^{-2}	8.49×10^{-3}	1.46×10^{-1}	6.33×10^0
Model6	1.5	6.64×10^{-2}	1.78×10^{-2}	1.94×10^{-1}	3.72×10^0
Model7	1.8	9.63×10^{-2}	4.27×10^{-2}	2.96×10^{-1}	2.26×10^0

TABLE 1

THE SHEAR RATES USED IN OUR PARAMETRIC SURVEY ARE LISTED IN THE FIRST COLUMN. THE SECOND, THIRD, AND FORTH COLUMN SHOW THE TIME- AND VOLUME-AVERAGED MAXWELL STRESS $\langle \langle w_M \rangle \rangle$, REYNOLDS STRESS $\langle \langle w_R \rangle \rangle$, AND MAGNETIC ENERGY $\langle \langle E_{\text{mag}} \rangle \rangle$ NORMALIZED BY THE INITIAL GAS PRESSURE $P_0 = 5 \times 10^{-7}$. THE RATIO OF MAXWELL AND REYNOLDS STRESSES $\langle \langle w_M \rangle \rangle / \langle \langle w_R \rangle \rangle$ IS IN THE FIFTH COLUMN. THE TIME-AVERAGE IS TAKEN OVER THE SATURATED STAGE FROM $50t_{\text{rot}}$ TO $150t_{\text{rot}}$ FOR MODELS 1,2,3, AND FROM $100t_{\text{rot}}$ TO $150t_{\text{rot}}$ FOR MODELS 4,5,6,7. MODEL 2 CORRESPONDS TO THE FIDUCIAL ONE.

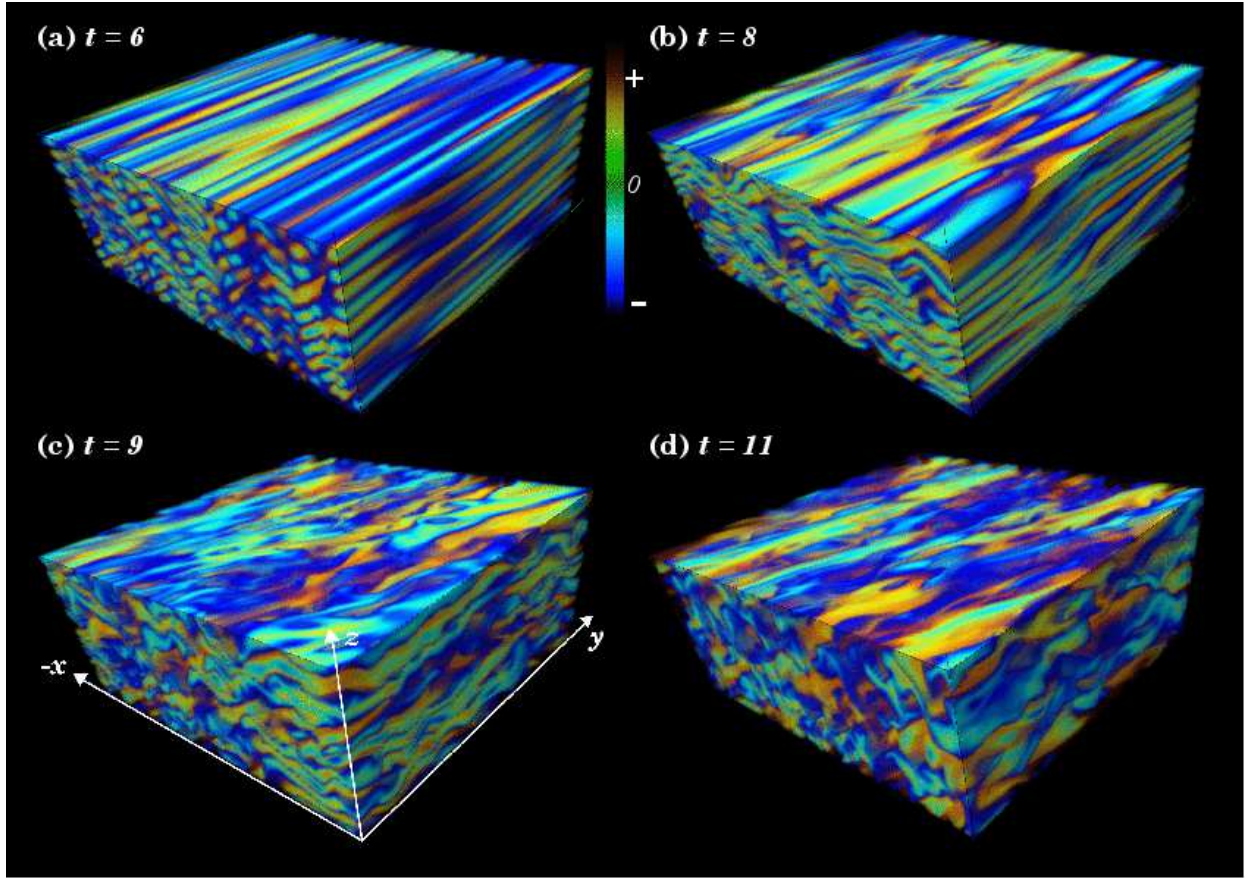


FIG. 3.— 3D Volume rendering of the radial magnetic field for the fiducial model at the times (a) $t = 6t_{\text{rot}}$, (b) $t = 8t_{\text{rot}}$, (c) $t = 10t_{\text{rot}}$, and (d) $t = 11t_{\text{rot}}$.

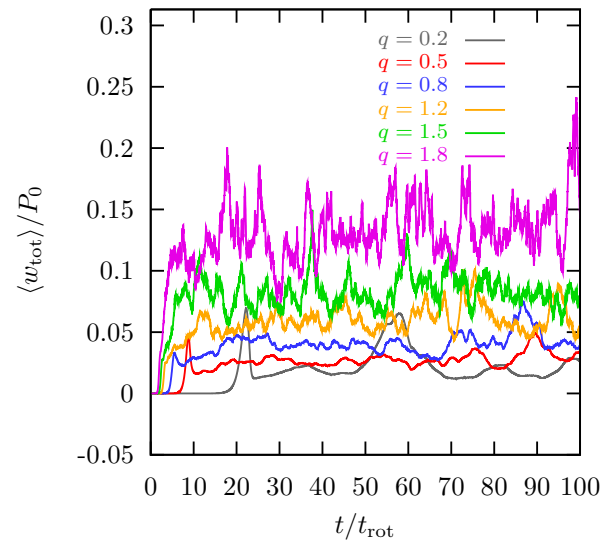


FIG. 4.— Temporal evolution of volume-averaged total stress $\langle w_{\text{tot}} \rangle$ normalized by the initial gas pressure P_0 for the models with different shear rates of $q = 0.2$ (grey), 0.5 (red), 0.8 (blue), 1.2 (orange), 1.5 (green) and 1.8 (purple) respectively.

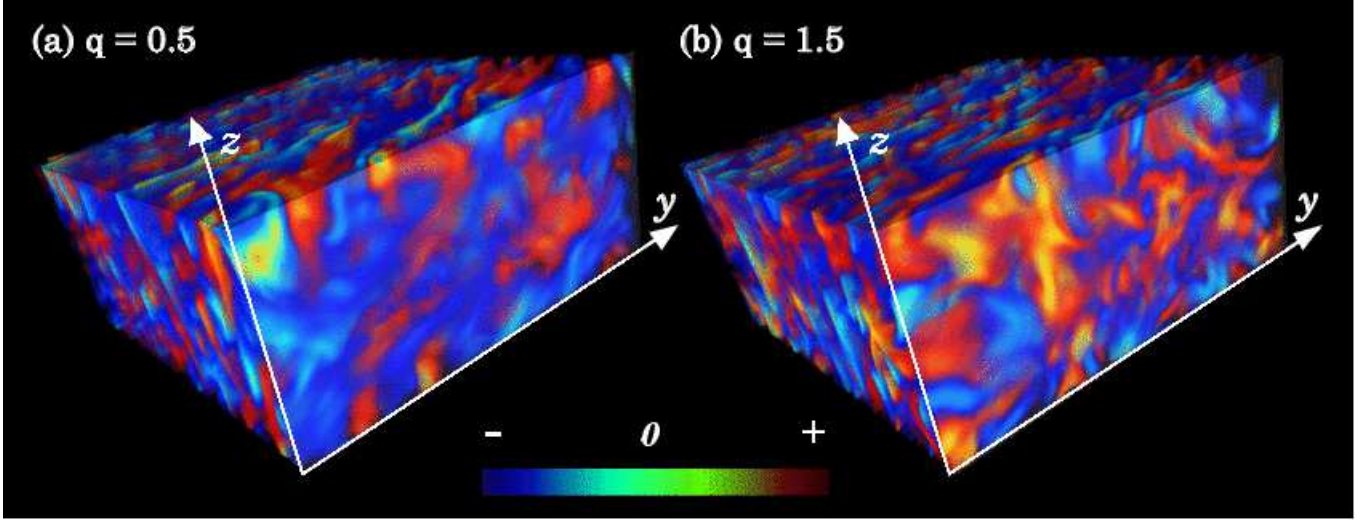


FIG. 5.— 3D volume rendering of the radial magnetic field for the models with (a) $q = 0.5$, and (b) $q = 1.5$. The color bar indicates the amplitude of the radial magnetic field, that is the red denotes the positive value and the blue is the negative.

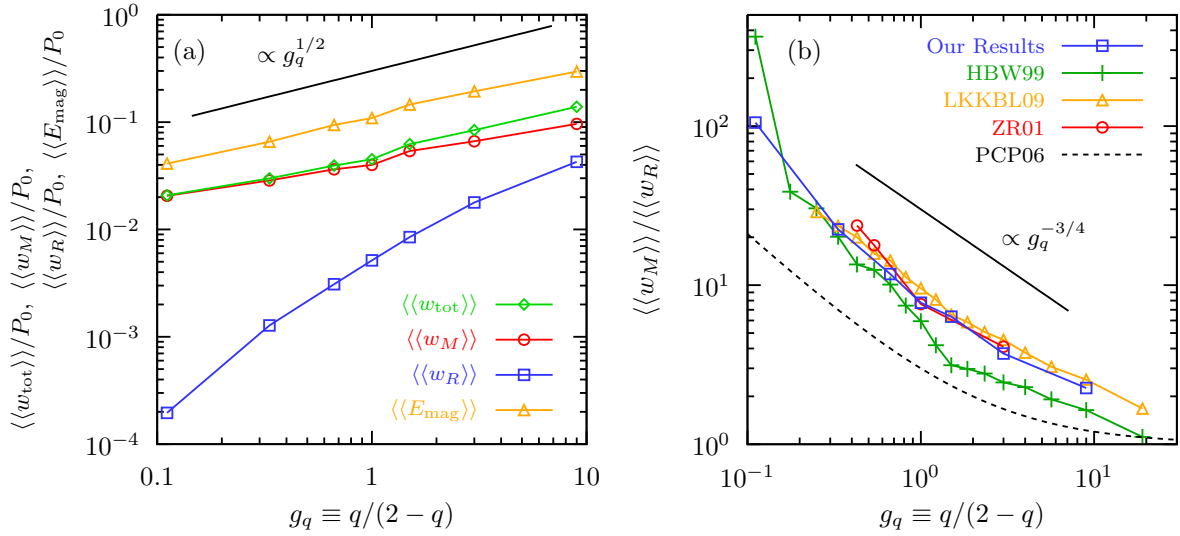


FIG. 6.— (a). The volume- and time-averaged Maxwell (red circles), Reynolds (blue squares) and total stresses (green diamonds) as a function of the shear-vorticity ratio g_q . The yellow triangles represent time- and volume- averaged magnetic energy at the saturated state. (b). The ratio of Maxwell and Reynolds stresses for the models with different initial settings as a function of the shear-vorticity ratio g_q . The blue squares, green crosses, yellow triangles, and red circles demonstrate the results of our work, Hawley et al. (1999), Liljeström et al. (2009), and Ziegler&Rudiger (2001) respectively. The dashed line traces the prediction from the local model developed by Pesah et al. (2006). The solid line gives a power law relation of $\langle\langle w_M \rangle\rangle/\langle\langle w_R \rangle\rangle \propto g_q^{-3/4}$.

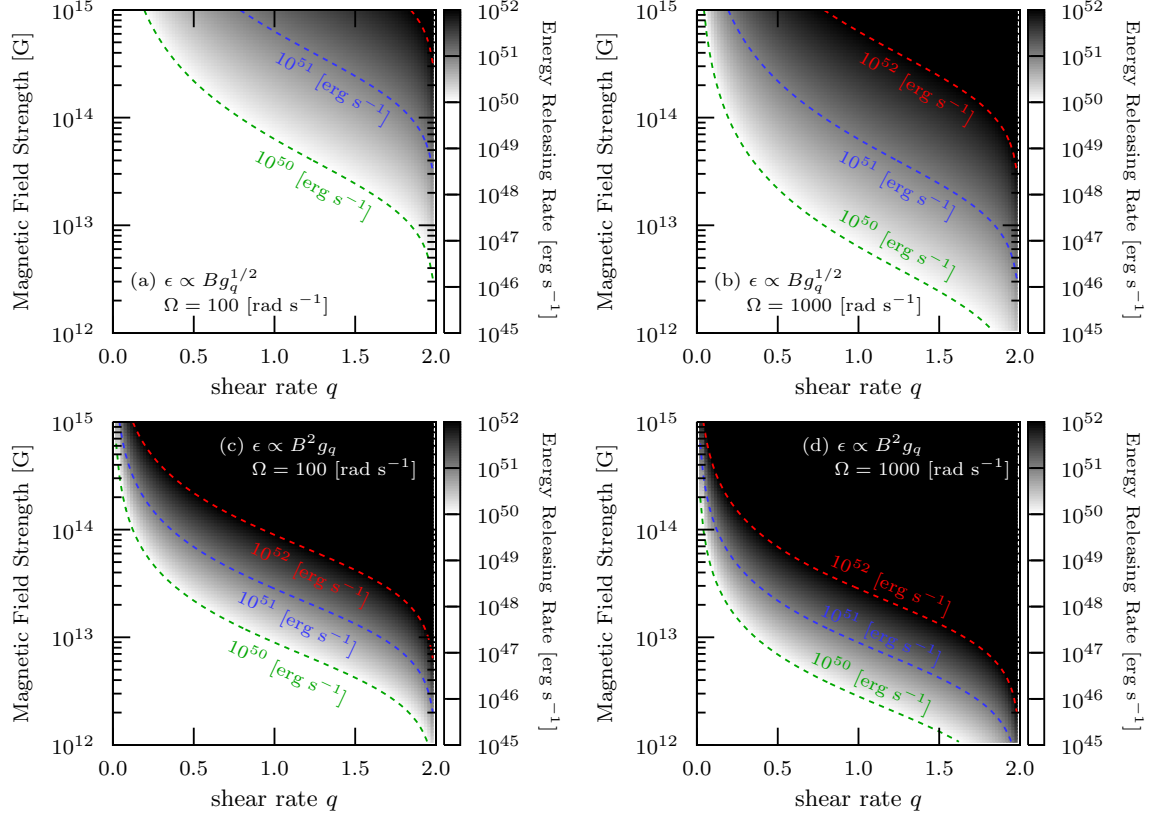


FIG. 7.— The energy releasing rate due to the MRI turbulence L_{MRI} as functions of the magnetic field strength B and the shear rate q . Panels (a) and (b) show the models with the weakest parameter dependence of $\xi = 1$ and $\delta = 1/2$, while Panels (c) and (d) are for the models with the strongest parameter dependence of $\xi = 2$ and $\delta = 1$. The slow rotation ($\Omega = 100 \text{ rad sec}^{-1}$) is assumed in left panels and the rapid rotation ($\Omega = 1000 \text{ rad sec}^{-1}$) is in right panels. The green, blue and red dashed curves correspond to the energy releasing rates 10^{50} , 10^{51} , and $10^{52} \text{ erg sec}^{-1}$ respectively. Note that the darker color gives the higher energy releasing rate.

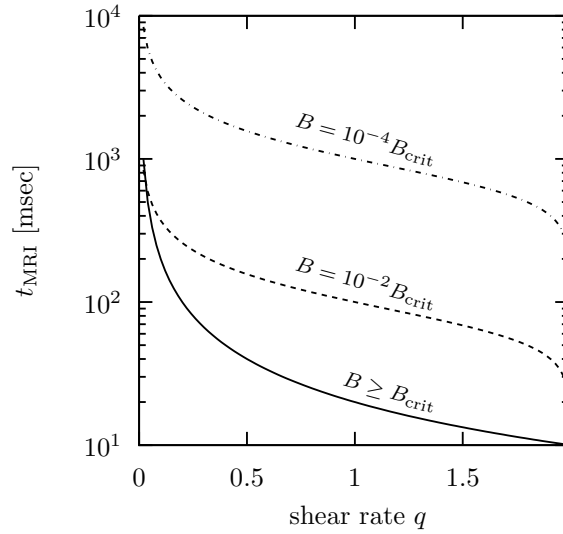


FIG. 8.— The typical linear growth time of the MRI as a function of the shear rate for the cases with $B \geq B_{\text{crit}}$ (solid line), $B = 10^{-2} B_{\text{crit}}$ (dashed line) and $B = 10^{-4} B_{\text{crit}}$ (dash-dotted line), where $B_{\text{crit}} = 3.5 \times 10^{12} \rho_{12}^{1/2} \nu_{10}^{1/2} \Omega_2^{1/2} \text{ [G]}$. We adopt the moderate spin rate of $\Omega = 100 \text{ rad sec}^{-1}$ in this figure.